J. Fluid Mech. (2001), *vol.* 443, *pp.* 271–292. Printed in the United Kingdom

Measurement and computation of hydrodynamic coupling at an air/water interface with an insoluble monolayer

By AMIR H. HIRSA[1], JUAN M. LOPEZ[2] AND REZA MIRAGHAIE[1]

[1]Department of Mechanical Engineering, Aeronautical Engineering and Mechanics, Rensselaer Polytechnic Institute, Troy, NY 12180, USA

[2]Department of Mathematics, Arizona State University, Tempe, AZ 85287, USA

(Received 18 October 2000 and in revised form 23 March 2001)

The coupling between a bulk vortical flow and a surfactant-influenced air/water interface has been examined in a canonical flow geometry through experiments and computations. The flow in an annular region bounded by stationary inner and outer cylinders is driven by the constant rotation of the floor and the free surface is initially covered by a uniformly distributed insoluble monolayer. When driven slowly, this geometry is referred to as the deep-channel surface viscometer and the flow is essentially azimuthal. The only interfacial property that affects the flow in this regime is the surface shear viscosity, μ^s, which is uniform on the surface due to the vanishingly small concentration gradient. However, when operated at higher Reynolds number, secondary flow drives the surfactant film towards the inner cylinder until the Marangoni stress balances the shear stress on the bulk fluid. In general, the flow can be influenced by the surface tension, σ, and the surface dilatational viscosity, κ^s, as well as μ^s. However, because of the small capillary number of the present flow, the effects of surface tension gradients dominate the surface viscosities in the radial stress balance, and the effect of μ^s can only come through the azimuthal stress. Vitamin K_1 was chosen for this study since it forms a well-behaved insoluble monolayer on water and μ^s is essentially zero in the range of concentration on the surface, c, encountered. Thus the effect of Marangoni elasticity on the interfacial stress could be isolated. The flow near the interface was measured in an optical channel using digital particle image velocimetry. Steady axisymmetric flow was observed at the nominal Reynolds number of 8500. A numerical model has been developed using the axisymmetric Navier–Stokes equations to examine the details of the coupling between the bulk and the interface. The nonlinear equation of state, $\sigma(c)$, for the vitamin K_1 monolayer was measured and utilized in the computations. Agreement was demonstrated between the measurements and computations, but the flow is critically dependent on the nonlinear equation of state.

1. Introduction

The dynamics of gas/liquid interfaces play an important role in many fields, ranging from biomedical applications such as lung surfactant therapy (Grotberg 1994) to manufacturing applications such as polyurethane foam stabilization (Snow, Pernisz & Stevens 1998). We are interested in investigating the coupling between the bulk (liquid) flow and the interface in the presence of surface-active materials, surfactants.

The coupling between the liquid subphase and the interface with surfactants has been the subject of numerous studies; many references to this subject are provided by Edwards, Brenner & Wasan (1991). For the most part, these studies have been restricted to the Stokes flow (inertialess) limit (e.g. Sacchetti, Yu & Schechter 1993; Schwartz, Knobler & Bruinsma 1994; Chen & Stebe 1996; Stone & Ajdari 1998; Johnson & Borhan 1999). While there have been several experimental studies (Warncke, Gharib & Roesgen 1996; Hirsa *et al.* 1997*a*) in which the free-surface boundary layer is resolved and theoretical/computational studies of the Navier–Stokes equations (Tsai & Yue 1995; Lopez & Chen 1998; Lopez & Hirsa 1998, 2000), the number of combined studies directly addressing the coupling with bulk flows that are not restricted to the Stokes flow are limited (Trygvasson *et al.* 1992). The experiments in Trygvasson *et al.* (1992) only included bulk flow measurements away from the interface and the free surface boundary layer was not resolved.

The interfacial coupling is a result of the bulk liquid's viscosity ensuring that the surfactant film at the interface has the same velocity as the bulk fluid at the interface. The coupling then formally comes about by equating (balancing) the shear stress in the liquid evaluated at the interface with that of the interface. The interfacial stress is determined from its constitutive relationship. The most widely used constitutive relation is the Boussinesq–Scriven surface model (Scriven 1960), appropriate for so-called Newtonian interfaces. In such a model, the interfacial stress tensor is composed of an elastic part, due to surface tension, and a viscous part, which is a linear function of the surface rate of strain. The viscous portion is composed of two parts, a shear and a dilatational component. Note that even for incompressible bulk fluids, the interfacial velocity will not be (surface) divergence-free in general. Even when the interface does not exhibit any intrinsic viscosity, the non-divergence-free nature of the interfacial velocity has important consequences for the hydrodynamic coupling, particularly with regard to the interfacial advection of surfactants (e.g. Stone & Leal 1990; Eggleton, Pawar & Stebe 1999). The resulting stress balance at the interface then provides the 'boundary' (interface) condition needed to solve the Navier–Stokes equations for the system as a whole.

When the interface is not far from equilibrium, it is reasonable to linearize about the equilibrium state. The majority of studies of interfacial coupling invoke such an assumption, treating the surface tension gradient and surface viscosities (if applicable) as constants. Eggleton *et al.* (1999) have shown, however, that even in the Stokes flow limit, the hydrodynamic coupling is very sensitive to nonlinearities in the equation of state, relating the surface tension to the thermodynamic state of the interface (through the surfactant concentration). With bulk flows that are not restricted to the Stokes limit, one can expect the interface to be more readily driven away from uniform surfactant coverage, making the precise form of the equation of state crucial for a correct description of the coupled system.

In the present study we test the appropriateness of a Newtonian surface constitutive relation for vitamin K_1, which forms an insoluble monolayer on water (Gaines 1966). For the range of concentrations used, we have determined that the surface shear viscosity is negligible, and for the range of capillary number considered the Marangoni stress dominates any contribution from the viscous resistance to surface dilations. So, the only issue to address is whether the nonlinear equation of state when incorporated into the constitutive relation gives the correct hydrodynamics. The vitamin K_1 monolayer is well behaved (Weitzel, Fretzdorff & Heller 1956), in the sense that measurements of the 'equation of state' obtained through the standard technique of surface compression in a Langmuir trough give essentially identical

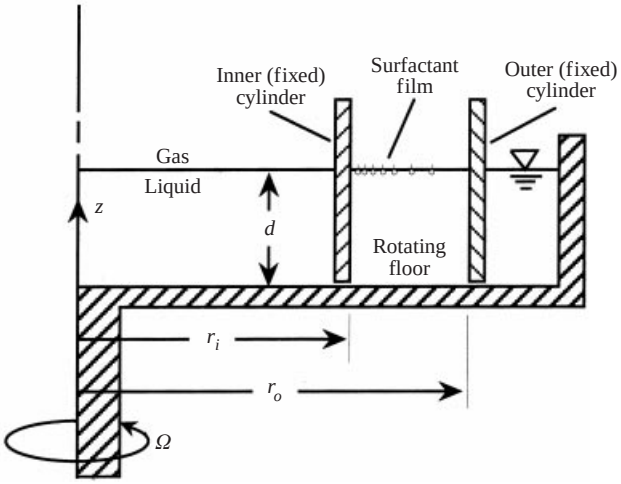

FIGURE 1. Schematic of the flow apparatus.

results to measurements during surface expansion over a wide range of initial and final surfactant concentrations. It is often taken for granted in theoretical studies that $\sigma(c)$ is a functional relationship, and hence the phrase 'equation of state', but in practice very few insoluble monolayers behave in exactly this way. The fact that vitamin K_1 does so is indicative of the absence of slow phase transitions and is consistent with the smooth (albeit nonlinear) shape of the equation of state measured for this insoluble and essentially inviscid monolayer.

The flow geometry that we use to study the hydrodynamic coupling was chosen so as to minimize the mechanisms involved and yet still be sensitive to the nonlinearities in the equation of state. The geometry corresponds to that of the deep-channel viscometer (Mannheimer & Schechter 1970), consisting of fluid bound between two concentric cylinders, and the flow is primarily driven by the constant rotation of the bottom endwall (see figure 1). On the free surface, a monolayer of insoluble surfactant is initially spread uniformly. We have determined a range of governing parameters in which the resultant flow remains axisymmetric and reaches steady state on a viscous time scale, and yet also produces a radial surface flow that is capable of compressing the monolayer over a range of initial concentrations. In this range of parameters, the free surface remains flat and the contact angle between the free surface and the cylinder sidewalls is 90°. That the flow remains steady and axisymmetric and the air/water interface flat results in relatively simple expressions for the tangential stress balances at the interface, thus making the measurements of the flow quantities to be compared with theory and numerics simpler to obtain.

Following a description of the experimental apparatus and procedures in the next section, the results of the velocity measurements are presented in § 3. The problem formulation along with numerical procedures for the solution are presented in § 4. The numerical results for various initial surfactant concentration are presented in § 5 along with comparisons to the measurements.

2. Experimental apparatus and methods

Doubly distilled (DD) water was used throughout the study. Tap water was first filtered using a 1 micron sediment filter, then pretreated prior to distillation using an

	Surface pressure ($dyn\,cm^{-1}$)				
Water sample	0 h	1 h	2 h	3 h	Resistivity ($M\Omega\,cm$)
Unseeded DD	0.10	0.10	0.16	0.16	6.6
Seeded DD	0.10	0.10	0.10	0.10	6.7
Commercial D	0.10	0.16	0.16	0.16	6.3
HPLC	0.16	0.16	0.32	0.64	5.6

TABLE 1. Surface pressure of various water samples of the indicated age, obtained by rapid compression. Note that the pH of all samples tested was indistinguishable and in the range 6.5–7.0, as expected for pure water.

organic removal filter (Barnstead, model D8904) and an ion removing filter (Barnstead, D8921). Following the pretreatment, the water was first distilled in a Stokes distiller (Water Distillers Inc., 171-E) and then in a glass second distiller (Corning, AG-1B). The water was handled only using HF acid-etched glass containers and dispensed from a Teflon squeeze bottle. The surface tension of the DD water was identical to the expected value (Weast 1980) within the experimental uncertainty ($\pm 0.05\,dyn\,cm^{-1}$). Table 1 shows a comparison of the surface pressure π (surface tension of the cleanest water minus the surface tension of the water in question) as a function of the age of the surface for the present DD water, HPLC-grade water (Aldrich, catalogue No. 27073-3), and commercial distilled water (Poland Springs). The surface pressure was measured in a Langmuir trough, described below, immediately following a rapid compression (10 : 1 compression in under 60 s). This was done in order to closely pack the residual surfactant molecules, making their presence more easily detectable before they can desorb from the interface. The relative purity of the present DD water is evident from table 1. For reference, the measured resistivity and pH of each water sample is also included in the table.

The interfacial property measurements for the vitamin K_1 monolayer on water were performed using established techniques. The surface tension was measured using a Wilhelmy plate and electrobalance (Nima, PS4). Filter paper (Nima) was used as the plate to ensure complete wetting. Surface tension measurements were made as a function of surfactant concentration in a Langmuir trough constructed of Teflon. Vitamin K_1 (Aldrich, 28740-7) was diluted with $99^{+}\%$ pure hexane (Aldrich, 13938-6) and spread using a glass microsyringe (Hamilton, 14813112). The cleanliness of the Langmuir trough and the purity of the hexane were established in the trough prior to measurements of the equation of state. The equation of state for the vitamin K_1 monolayer, at temperature $23 \pm 1\,^{\circ}C$, is shown in figure 2(*a*). A close-up of the data is shown in figure 2(*b*). The error in the measurement of surface tension has been estimated to be less than $\pm 0.05\,dyn\,cm^{-1}$ and the error in the measurement of surfactant concentration is less than $\pm 5\%$.

The other interfacial properties required for the interfacial stress balance are the surface shear viscosity, μ^s, and surface dilatational viscosity, κ^s. Established techniques are available for the measurement of μ^s. The surface shear viscosity for a vitamin K_1 monolayer was measured using a standard deep-channel surface viscometer (Edwards *et al.* 1991). This surface viscometer was constructed of stainless steel and had dimensions similar to that introduced by Mannheimer & Schechter (1970). For the range of concentration used in this study (less than $1.5\,mg\,m^{-2}$), vitamin K_1 exhibited no detectable surface shear viscosity. The deep-channel surface viscometer is sensitive

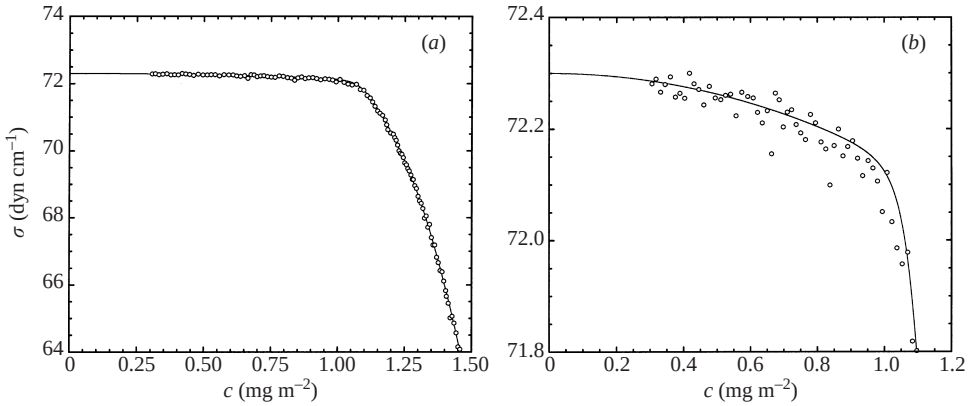

FIGURE 2. (*a*) Equation of state, $\sigma(c)$, for a vitamin K_1-water system measured using a Langmuir trough (symbols) together with a nonlinear curve fit given by (4.14); (*b*) close-up of (*a*).

down to approximately $10^{-4}\,\mathrm{g\,s^{-1}}$ (surface Poise), therefore the dimensionless surface shear viscosity ($\mu^s/\mu r_o$, where μ is viscosity in the bulk and r_o is the outer radius, nominally 10 cm) is less than 10^{-3} and thus neglected. The surface dilatational viscosity has not yet been measured consistently with any two different experimental techniques for any surfactant (Edwards *et al.* 1991). However, for the flows investigated here, the capillary number is so low that surface dilitational effects are negligible compared to the surfactant Marangoni stress (Lopez & Hirsa 2000).

Figure 3 shows a schematic of the optical channel in which the velocity was measured. The floor of the channel consists of an optical window, which is rotated by a computer controlled stepping motor. The water is contained by a cast acrylic cylinder bonded to the glass floor. The inner and outer cylinders consist of 2.5 cm high cast acrylic tube, with radii $r_i = 7.62 \pm 0.01$ cm and $r_o = 9.82 \pm 0.01$ cm. The thickness of the (stationary) outer cylinder was minimized (≈ 0.3 cm) to reduce optical distortion. The stationary cylinders were press-fitted into grooves precision machined in the cover which held them at 0.0076 ± 0.005 cm above the rotating floor. The tolerance in the gap (± 0.005 cm) was primarily due to the finite wobble of the rotating floor. A groove was machined on each cylinder at 1.1 cm from the bottom (not shown in figure 1) in order to fix the location of the contact line. Paraffin from a hexane solution was deposited in the groove to ensure that the water wetted the cylinder walls only up to the bottom of the groove. Thus, by filling water in the container to a depth of 1.1 cm, a 90° contact angle was achieved resulting in a flat air/water interface in the 2.2 cm wide region between the cylinders. The depth-to-gap ratio, $\Lambda = d/(r_o - r_i) = 0.5$ and the radius ratio $r_i/r_o = 0.776$.

The velocity measurements were primarily performed in the meridional plane (r, z), see figure 3, where the radial and vertical velocity components, u and w, were obtained and the azimuthal vorticity, η, determined. Due to the relatively high magnification of the DPIV imaging system (as high as $63\,\mathrm{pixels\,mm^{-1}}$), it was necessary to avoid the optical distortion that would occur by viewing the illuminated meridional plane through the rotating container. The variations in the thickness and radius of the rotating container can result in time-dependent refraction. To avoid viewing through the rotating cylinder, a periscope setup was devised to permit viewing the meridional plane from between the fixed outer cylinder and the rotating cylinder. As depicted in figure 3, a right prism was partially submerged in the water outside of the fixed

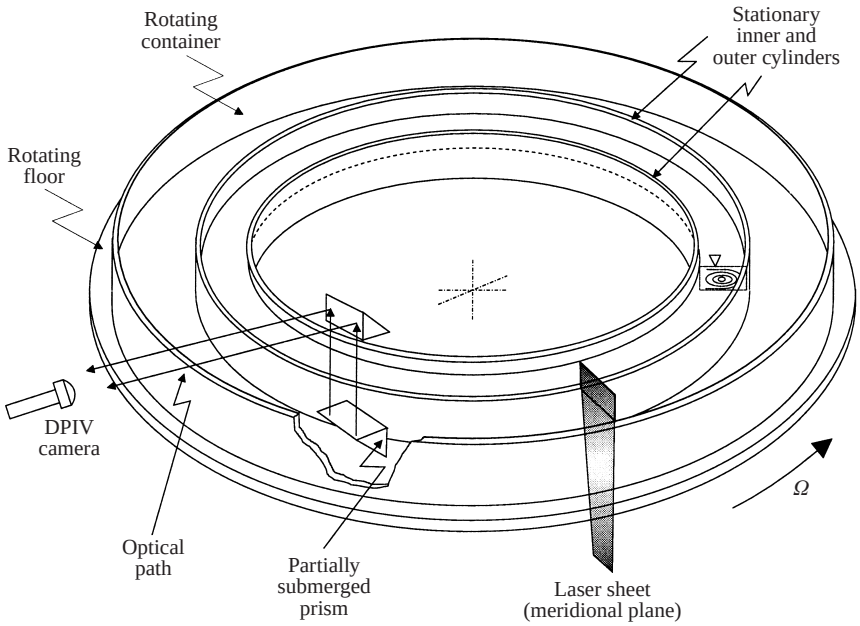

FIGURE 3. Schematic of the optical channel showing the stationary cylinders, rotating container, and the optical setup. The prisms were only used for measurements in the meridional plane which is illuminated by a vertical laser sheet.

outer cylinder and held stationary. A second right prism was held stationary above the partially submerged prism to allow horizontal viewing with the camera. For the measurements in the meridional plane, a vertical laser light sheet with a thickness of 0.1 cm was directed upward through the optical floor. For measurements in the plane of the surface ($z = d$), a horizontal light sheet with a thickness of less than 0.05 cm was directed radially inward. The illuminated horizontal plane was imaged from beneath the channel using a mirror at 45° held stationary below the rotating optical floor.

The technique of digital particle image velocimetry (DPIV) utilized here has been presented elsewhere (Logory, Hirsa & Anthony 1996; Hirsa *et al.* 1997*b*), as has the method of boundary-fitted DPIV (Hirsa, Vogel & Gayton 2001; Vogel *et al.* 2001) used for resolving the interfacial velocity and vorticity in meridional plane measurements, and so will be not be repeated here. However, the preparation of the seeded water required special attention to achieve the requisite level of purity and is described here in some detail. Polystyrene particles stabilized with surface-bound sulphate groups were used for this experiment. For high magnification measurements (63 pixels mm^{-1}) in the meridional plane, 3 micron particles (Aldrich, 45941-0) were utilized. For measurements in the surface plane (22 pixels mm^{-1}), particles of 11.9 micron diameter (Aldrich, 45942-9) were used. Both of these particles can be thoroughly cleaned without causing them to form clusters. The seeding particles, which were received in a water suspension were first rinsed with HPLC isopropyl alcohol (2-propanol; Aldrich, 27049-0). This was accomplished by withdrawing a volume of the particle suspension (10% solid) and depositing it in a test tube partially filled with the isopropyl alcohol; 0.2 ml of the 3 micron or 0.5 ml of the 11.9 micron particle suspension was used. The test tube was then centrifuged and the liquid was aspirated leaving the wet seeding particles at the bottom. Fresh isopropyl alcohol was then added to the test tube and

the contents were thoroughly shaken by submersion in an ultrasonic cleaner bath. The test tube was then centrifuged and the isopropyl alcohol was aspirated. The cleaning process (solvent addition, ultrasonic shaking, centrifuge, followed by aspiration) was then repeated twice with HPLC methanol (Aldrich, 27047-4) and four times with DD water. The cleaned particles were added to a 4 l conical flask filled with DD water. As a final step in removing surfactants from the seeded water, pure nitrogen bubbles (generated from liquid nitrogen boil-off) were introduced from a Pyrex gas dispersion disc (Fisher Scientific, 11-137F). Residual surfactants are adsorbed on the nitrogen bubbles (e.g. see Scott 1975) and brought to the surface where they are continuously aspirated and fresh DD water was added at a rate of $1\,l\,h^{-1}$ to maintain a constant water level. This process was continued for at least 1 hour. The resulting water was seeded with less than 4 p.p.m. (by volume and mass) of clean polystyrene particles. Surface pressure measurements of the seeded water, presented in table 1, demonstrate the effectiveness of the cleaning process, including the bubbling with nitrogen gas. Ultimately, however, the success of the cleaning process was evaluated in the optical channel via measurements of the radial surface velocity at the interface without a deposited monolayer.

3. Results of velocity field measurements

The interfacial flow measurements were performed with the floor rotating at $\Omega = 0.843\,\mathrm{rad\,s^{-1}}$. The resulting Reynolds number $Re = \Omega r_o^2/\nu = 8.5 \times 10^3$, where ν is the kinematic viscosity ($9.35 \times 10^{-3}\,\mathrm{cm^2\,s^{-1}}$ for water at 23 °C). The capillary number, $Ca = \mu\Omega r_o/\sigma_o = 10^{-3}$, where μ is the dynamic viscosity in the bulk ($9.33 \times 10^{-3}\,\mathrm{g\,cm^{-1}\,s^{-1}}$) and $\sigma_o = 72.4\,\mathrm{dyn\,cm^{-1}}$ is the surface tension for clean water at this temperature.

Since strong secondary flow requires relatively large Re (Lopez & Hirsa 1998), a stability study was first undertaken to determine the margin of stability at the present Reynolds number. The flow in a meridional plane was measured with DPIV at the location $z/d = 0.5$ and $x = (r - r_i)/(r_o - r_i) = 0.25$. This location in the core of the flow was selected because the velocity is adequately large to avoid excessive noise from the DPIV analysis, and is outside of the wall boundary layers where disturbances tend to be dampened. Figure 4 shows the root-mean square of the vertical velocity, w_{rms}, non-dimensionalized with Ωr_o. Measurements taken on three different days (labelled Series 1–3) are shown for Reynolds number between 4000 and 14 000 (by varying Ω). The expected level of noise from the DPIV system, computed based on uncertainty of 0.2 pixels for velocity squared (0.1 pixels for velocity) is shown for reference. Comparison between the measured and the expected noise level illustrates that the flow is essentially steady, and hence axisymmetric, for Re up to about 12 000. For $Re = 8500$, the value used for the interfacial measurements, the flow reached an axisymmetric steady state following a constant-acceleration start-up (for 27 s from rest) within about 100 s. This is the diffusive time scale through the depth of the bulk fluid.

The radial velocity distribution at the interface ($z = d$), $u^s(x)$, obtained via boundary-fitted DPIV measurements in a meridional plane, is shown in figure 5 for c_0 up to $1.0\,\mathrm{mg\,m^{-2}}$. The velocity data are non-dimensionalized with Ωr_o and shown as a function of the dimensionless gap, x. In the absence of a deposited monolayer ($c_0 = 0$), the surface is clean except for a narrow region near the inner cylinder. Residual contamination tends to accumulate on the interface near the inner cylinder due to the action of secondary flow in the bulk. The flow field, including the secondary flow in the bulk, is described in some detail in § 5. The residual contamination diminishes the radially inward velocity faster than would otherwise occur in an

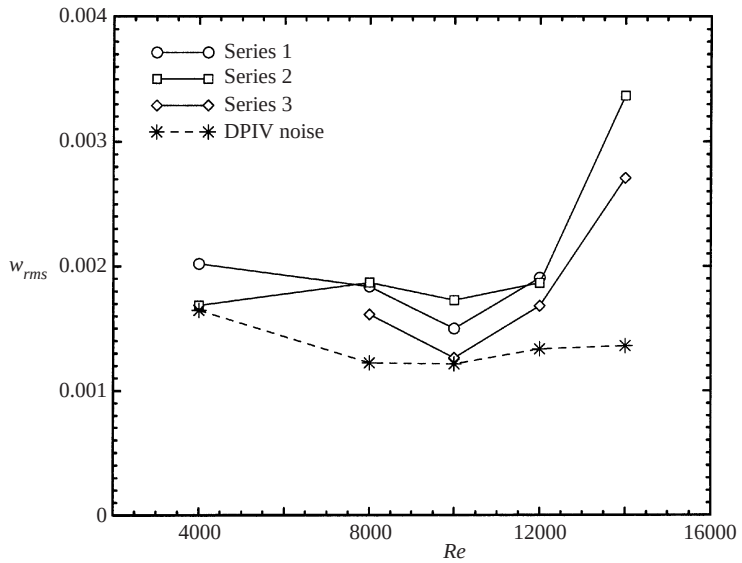

FIGURE 4. Root-mean-square of the vertical velocity, scaled by Ωr_o, at the point $(r-r_i)/(r_o-r_i) = 0.25$, $z/d = 0.5$ measured on three separate days (Series 1–3) over a range of Re, together with the noise level from the DPIV system (dashed line).

absolutely clean medium. The contaminated region is approximately 0.2 cm wide or less than 10% of the gap. The extent of the velocity measurements in the meridional plane was limited in the region $x \to 1$ by the optical distortion due to the curvature of the outer cylinder near r_o. Data in this plane will only be presented up to $x = 0.85$. For the $c_0 = 0$ case, the peak interfacial velocity in the radial direction is -0.145 and occurs at approximately $x = 0.6$. The spatial resolution of these measurements, based on the final cross-correlation window (16 pixels), is 0.025 cm or approximately 1% of the gap and 2% of the depth. The resolution of the measurements, which amounts to spatial filtering, is especially important when comparing the experimental results to computations (see § 5).

As part of the boundary-fitted DPIV technique utilized for velocity measurements in the meridional plane, the location of the free surface is determined. The measurements showed that the extent of surface deformation, from the highest point to the lowest, was less than 50 microns. The accuracy of this measurement is approximately ± 10 microns, corresponding to approximately 0.5 pixel. Thus, the surface is found to be relatively flat, with the maximum departure from the undisturbed surface of only 0.2% of the depth. The measured deformation is consistent with the deformation estimated from the Froude number, $Fr = \Omega^2 r_o^2/gd$ of order 10^{-2} for $Re = 8500$.

The measured radial velocity distribution is in qualitative agreement with earlier calculations for a similar geometry and Re but for a different surfactant system (Lopez & Hirsa 2000). Flow calculations for the vitamin K_1 case are presented in the following sections. Figure 5 shows that with increasing initial concentration of the vitamin K_1 monolayer, the radial flow diminishes as the monolayer is accumulated toward the inner cylinder. A slight increase in the magnitude of the peak velocity can be observed for finite c_0 up to 0.4. It is apparent that the radial velocity diminishes for $c_0 > 0.8\,\mathrm{mg\,m^{-2}}$ and the vitamin K_1 monolayer covers the entire measurement region.

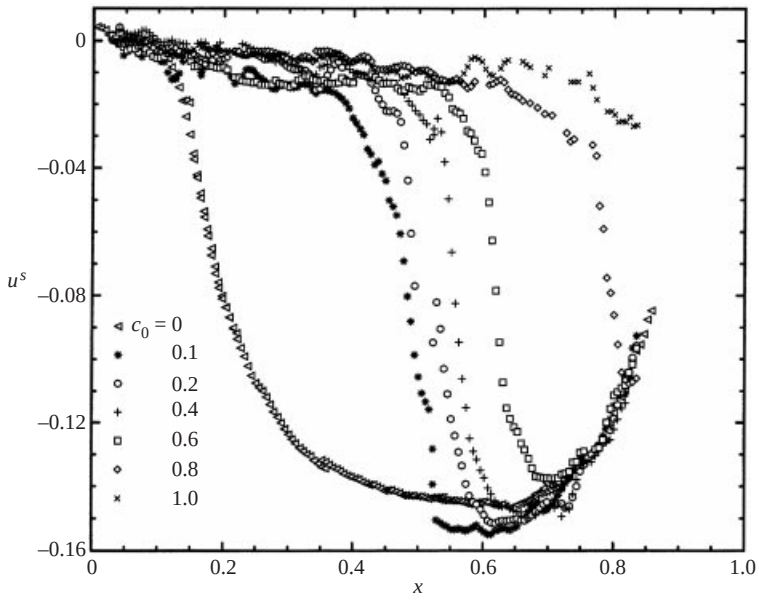

FIGURE 5. Radial velocity profile at the interface, $u^s(x)$, measured via boundary-fitted DPIV at steady state for various c_0 as indicated and $Re = 8500$.

The azimuthal vorticity distribution at the surface, $\eta^s(x)$, also determined from the boundary-fitted DPIV measurements in the meridional plane, is presented in figure 6. The vorticity is non-dimensionalized with Ω. The presence of a surfactant front is evident for $c_0 \lesssim 0.8\,\mathrm{mg\,m^{-2}}$. The vorticity exhibits an asymptotic behaviour toward r_i, as the initial surfactant surface concentration is increased. The extent of the asymptotic region increases with initial concentration. The spatial resolution of the azimuthal vorticity data is approximately 0.05 cm or 2% of the gap and 4% of the depth.

The azimuthal velocity distribution at the surface, $v^s(x)$, was measured with DPIV by placing a thin horizontal light sheet at the air/water interface. The finite thickness of the light sheet ($\lesssim 0.05$ cm) produces some depth-averaging of the data. The azimuthal velocity v^s, non-dimensionalized with Ωr_o, is presented in figure 7. The figure shows that for $c_0 = 0$ the azimuthal velocity increases rapidly with r to about 0.45 at $x = 0.15$ and then gradually decreases. The azimuthal velocity distribution changes little for c_0 between 0.1 and $1\,\mathrm{mg\,m^{-2}}$. This is consistent with the fact that μ^s is negligible in this range of c_0, and that the radial flow changes most drastically between $c_0 = 0$ and $c_0 = 0.1\,\mathrm{mg\,m^{-2}}$. The optical setup for these measurements in the plane of the surface permitted a slightly wider range of the gap to be viewed (x up to 0.9) than in the meridional plane (cf. figure 5).

4. Theoretical considerations

4.1. *Governing equations*

Having established that the flows of interest in this study remain axisymmetric, we project the governing equations onto an axisymmetric subspace. The governing equations are the axisymmetric Navier–Stokes equations, together with the continuity equation and appropriate boundary and initial conditions. Using a cylindrical polar coordinate system (r, θ, z), the Stokes streamfunction, ψ, the axial angular momentum,

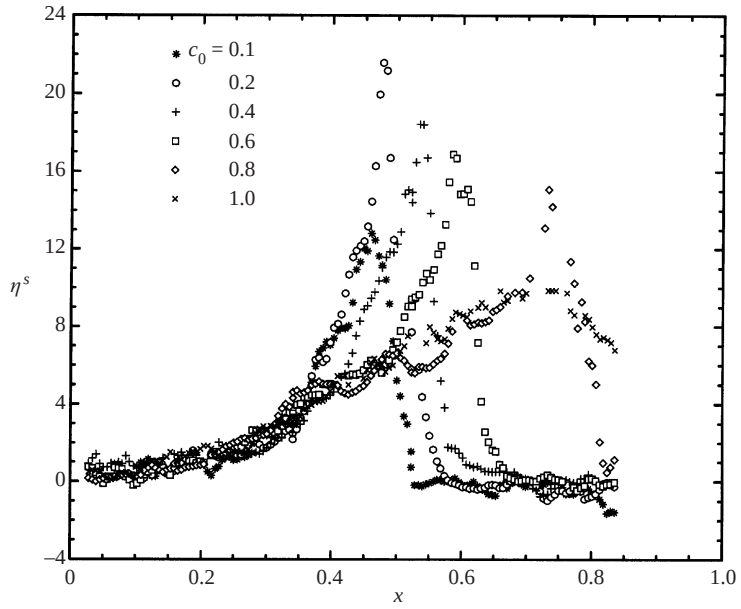

FIGURE 6. Azimuthal vorticity profile at the interface, $\eta^s(x)$, measured via boundary-fitted DPIV at steady state for various c_0 as indicated and $Re = 8500$.

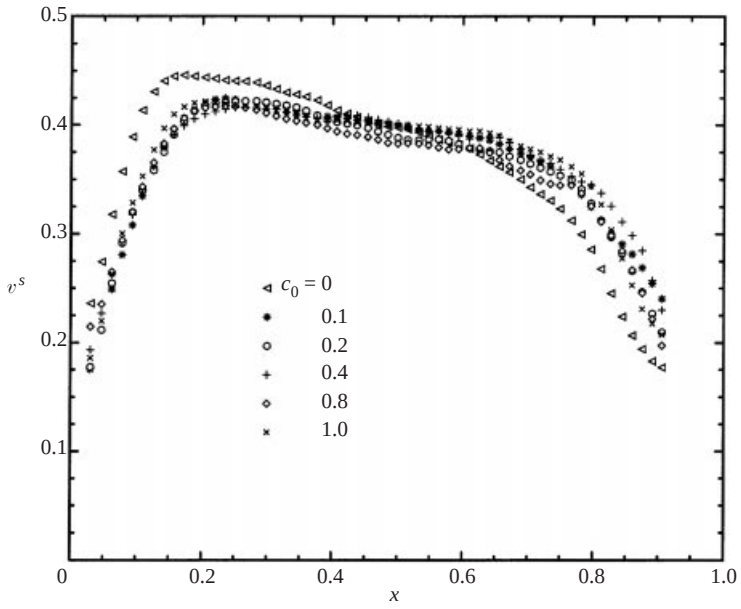

FIGURE 7. Azimuthal velocity profile at the interface, $v^s(x)$, measured via DPIV at steady state for various c_0 as indicated and $Re = 8500$.

α, and the azimuthal component of vorticity, η, the non-dimensional velocity vector is

$$\boldsymbol{u} = (u, v, w) = \left(-\frac{1}{r}\frac{\partial \psi}{\partial z}, \frac{\alpha}{r}, \frac{1}{r}\frac{\partial \psi}{\partial r} \right), \tag{4.1}$$

and the corresponding vorticity vector is

$$\nabla \times \boldsymbol{u} = \left(-\frac{1}{r}\frac{\partial \alpha}{\partial z}, \eta, \frac{1}{r}\frac{\partial \alpha}{\partial r} \right). \tag{4.2}$$

The use of ψ and α is convenient in axisymmetric swirling flows; contours of ψ in an (r, z)-plane depict the streamlines of the flow, and contours of α in that plane depict the vortex lines. Recall that vortex lines cannot begin or end at a stationary solid wall, they must be tangential to it, and at a flat stress-free (e.g. clean) gas/liquid interface the vortex lines are normal to it.

Using r_o as the length scale and $1/\Omega$ as the time scale, the non-dimensionalized axisymmetric Navier–Stokes equations are

$$\frac{\mathrm{D}\alpha}{\mathrm{D}t} = \frac{1}{Re}\nabla_*^2 \alpha, \tag{4.3}$$

$$\frac{\mathrm{D}\eta}{\mathrm{D}t} + \frac{\eta}{r^2}\frac{\partial \psi}{\partial z} - \frac{1}{r^3}\frac{\partial \alpha^2}{\partial z} = \frac{1}{Re}\left(\nabla^2 \eta - \frac{\eta}{r^2} \right), \tag{4.4}$$

where

$$\nabla_*^2 \psi = -r\eta, \tag{4.5}$$

$$\frac{\mathrm{D}}{\mathrm{D}t} = \frac{\partial}{\partial t} - \frac{1}{r}\frac{\partial \psi}{\partial z}\frac{\partial}{\partial r} + \frac{1}{r}\frac{\partial \psi}{\partial r}\frac{\partial}{\partial z}, \tag{4.6}$$

$$\nabla^2 = \frac{\partial^2}{\partial z^2} + \frac{\partial^2}{\partial r^2} + \frac{1}{r}\frac{\partial}{\partial r}, \tag{4.7}$$

and

$$\nabla_*^2 = \frac{\partial^2}{\partial z^2} + \frac{\partial^2}{\partial r^2} - \frac{1}{r}\frac{\partial}{\partial r}. \tag{4.8}$$

The boundary conditions on the solid boundaries are no-slip, i.e. the normal and tangential derivatives of ψ vanish; $\alpha = 0$ on the stationary cylinder walls and $\alpha = r^2$ on the rotating floor. The azimuthal vorticity η on the solid boundaries is determined by evaluating (4.5) on the boundaries once ψ is known. On the air/water interface, being a material surface, ψ is continuous with its value on the sidewalls, which we set to zero without loss of generality. Consistent with the measurements, we shall assume that the interface is flat, and hence the contact angle at the air/water/solid contact line is 90°. The conditions for α and η on the interface remain to be specified.

Our treatment of the interface considers the Boussinesq–Scriven surface fluid model for a Newtonian gas/liquid interface (Boussinesq 1913; Scriven 1960; Aris 1962; Slattery 1990), where the surface stress tensor is

$$\boldsymbol{T}^s = \sigma \boldsymbol{I}_s + \boldsymbol{S}^s = (\sigma + (\kappa^s - \mu^s)\mathrm{div}_s \boldsymbol{u}^s)\boldsymbol{I}_s + 2\mu^s \boldsymbol{D}^s, \tag{4.9}$$

and the viscous part of the surface stress tensor, $\boldsymbol{S}^s$, is described as a linear function of the surface rate of deformation tensor

$$2\boldsymbol{D}^s = \nabla_s \boldsymbol{u}^s \cdot \boldsymbol{I}_s + \boldsymbol{I}_s \cdot (\nabla_s \boldsymbol{u}^s)^T. \tag{4.10}$$

In this constitutive equation, κ^s is the surface dilatational viscosity, μ^s is the surface shear viscosity, σ is the thermodynamic (equilibrium) surface tension, $\boldsymbol{u}^s$ is the surface velocity vector, div_s is the surface divergence operator, ∇_s is the surface gradient operator, and $\boldsymbol{I}_s$ is the tensor that projects any vector onto the interface (for the flat interface considered in this study, $\boldsymbol{I}_s$ is the identity). This formulation allows the surface viscosities to vary with the surfactant concentration; this is important when

considering certain surfactants, such as hemicyanine (Lopez & Chen 1998; Hirsa 1998, 2000). We also allow for a nonlinear equation of state, $\sigma(c)$. A description of the general formulation is given in Lopez & Hirsa (2000).

Due to the vanishingly small measured values of μ^s for the range of surfactant concentrations encountered in the experiments and the relatively small Ca, μ^s and κ^s may be neglected for this study. The azimuthal stress balance, written in terms of non-dimensional α, then reduces to

$$\frac{\partial \alpha}{\partial z} = 0, \tag{4.11}$$

which says that vortex lines meet the air/water interface normally. The radial stress balance, in terms of non-dimensional η^s reduces to

$$\eta^s = \frac{1}{Ca}\frac{\partial \bar{\sigma}}{\partial r}, \tag{4.12}$$

which says that the radial stress balance is solely due to surface tension gradients, i.e. the (surfactant) Marangoni stress. Note that $\bar{\sigma}$ denotes the non-dimensionalized surface tension, defined below.

Since the surface tension, σ, is a function of the surfactant concentration c, we need to solve an active scalar advection–diffusion equation for c on the interface:

$$\frac{\partial c}{\partial t} = \frac{1}{r}\frac{\partial}{\partial r}\left(c\frac{\partial \psi}{\partial z}\right) + \frac{1}{Pe^s}\left(\frac{\partial^2 c}{\partial r^2} + \frac{1}{r}\frac{\partial c}{\partial r}\right), \tag{4.13}$$

where $Pe^s = \Omega r_o^2/D^s$ is the surface Péclet number and D^s is the surface diffusion of the surfactant; D^s is estimated to be of order $10^{-5}\,\mathrm{cm^2\,s^{-1}}$ for typical surfactants (Agrawal & Neuman 1988). In our experiments, $\Omega r_o^2 = 81.3\,\mathrm{cm^2\,s^{-1}}$, and in the computations we use $Pe^s = 10^5$. At the contamination front, the large gradients in concentration lead to a large production in surface azimuthal vorticity, resulting in a spike in η^s whose width scales with $1/\sqrt{Pe^s}$.

The nonlinear equation of state used in the computations is a fit to the experimentally measured surface tension of vitamin K_1 on a water substrate, as detailed in § 2. Figure 2 show this nonlinear fit along with the experimental measurements. The fit has the form

$$\sigma(c) = \sigma_0\bar{\sigma}(c) = \frac{a_2 + a_3 c + a_4 c^2}{1 + \exp(a_0 a_1 - a_1 c)} + \frac{a_5 + a_6 c^2}{1 + \exp(a_1 c - a_0 a_1)}, \tag{4.14}$$

where $\sigma_0 = 72.4$, $a_0 = 1.108$, $a_1 = 32.37$, $a_2 = 20.11$, $a_3 = 97.04$, $a_4 = -45.9$, $a_5 = \sigma_0$, and $a_6 = -0.15$; note σ_0 has the unit $\mathrm{dyn\,cm^{-1}}$ ($\mathrm{mN\,m^{-1}}$).

4.2. *Numerical technique*

Due to the nonlinear coupling between the bulk flow and the boundary conditions, an explicit time integration is implemented. We begin by discretizing in space using second-order centred differences. Equations (4.3) and (4.4) then have the form

$$\frac{\mathrm{d}\alpha_{i,j}}{\mathrm{d}t} = RHS_1(\alpha, \psi), \tag{4.15}$$

and

$$\frac{\mathrm{d}\eta_{i,j}}{\mathrm{d}t} = RHS_2(\eta, \alpha, \psi). \tag{4.16}$$

The computational domain is $r \in [r_i/r_o, 1]$, $z \in [0, d/(r_o - r_i)]$ with $r = r_i/r_o + i(r_o - r_i)/r_o n_r$ for $i \in [0, n_r]$, and $z = jd/r_o n_z$ for $j \in [0, n_z]$. Note that results will be

presented in terms of $x = (r - r_i)/d$. All the computations were done using $n_r = 600$, $n_z = 300$, $\delta t = 2 \times 10^{-4}$, $d/(r_o - r_i) = 0.5$, and $r_i/r_o = 0.776$. This fine resolution is more than sufficient to produce grid-independent results for the bulk flow. The need for such fine resolution stems from the use of a relatively high $Pe^s = 10^5$, as when a surfactant front forms for a range of parameters, the azimuthal vorticity at the interface has a sharp spike that necessitates the fine resolution. The usual tests where the grid spacing and time-step are halved have been performed, and it has been determined that the resolution used gives asymptotically converged results.

Starting from the initial conditions, the interior values of $\alpha_{i,j}$ and $\eta_{i,j}$ ($i \in [1, n_r - 1]$ and $j \in [1, n_z - 1]$) are evolved forward in time using a second-order predictor–corrector scheme. Denoting the current time by superscript k, the predictor stage by superscript $*$, and the next (corrected) stage by $k + 1$, we first evaluate

$$\alpha^*_{i,j} = \alpha^k_{i,j} + \delta t RHS^k_1, \tag{4.17}$$

and

$$\eta^*_{i,j} = \eta^k_{i,j} + \delta t RHS^k_2. \tag{4.18}$$

At this stage, we need to solve the elliptic equation (4.5) for ψ^* with the interior points for η^* just computed. Then, the surfactant concentration is advected by this streamfunction. So (4.13) is solved for c^* with ψ^*, and the boundary conditions $\partial c/\partial r = 0$ at $r = r_i/r_o$ and 1 (thus conserving total surfactant on the interface). This evolution is also done by the predictor–corrector scheme. One needs to do the full two stages to get from c^k to c^{**} to c^*, both stages using ψ^*. With $c^*(r)$, we evaluate $\partial\bar{\sigma}(c^*(r))/\partial r$. The boundary conditions for α^* and η^* are then evaluated. On the no-slip boundaries, this is straightforward. For the interface, we solve for α by using one-sided differences to discretize (4.11). Equation (4.12) gives η^s directly from the surface tension gradient. We now have everything (α, η, ψ, and c) at the predictor stage, and can repeat the whole process to obtain the corrector stage. We evolve α and η using

$$\alpha^{k+1}_{i,j} = 0.5(\alpha^k_{i,j} + \alpha^*_{i,j} + \delta t RHS^*_1), \tag{4.19}$$

and

$$\eta^{k+1}_{i,j} = 0.5(\eta^k_{i,j} + \eta^*_{i,j} + \delta t RHS^*_2). \tag{4.20}$$

5. Numerical results and discussion

5.1. *Comparison of clean surface measurements and computations*

The computed profiles of the radial and azimuthal velocity on the surface for the clean case ($c_0 = 0$) are presented in figures 8(*a*) and 8(*b*), respectively. The measured velocity profiles are also plotted in the figures. The results show good agreement between the measurements and the calculations for the clean interface except for a narrow region near the inner cylinder ($x = 0$) where residual surfactants which are inevitable in any experiment diminish the radial velocity and, in turn, alter the azimuthal velocity. For comparison, the computed profiles for a case with a minute amount of vitamin K_1 initially on the surface ($c_0 = 0.05\,\mathrm{mg\,m^{-2}}$) are also shown. Figure 8(*a*) shows that the measured radial velocity becomes zero at $x = 0.1$, compared to the computed $c_0 = 0.05\,\mathrm{mg\,m^{-2}}$ case in which the radial velocity diminishes at $x = 0.2$. The plots illustrate that the residual surfactants in the experimental flow, in general expected to be soluble, are comparable to less than $0.05\,\mathrm{mg\,m^{-2}}$ of vitamin K_1 monolayer spread uniformly on the surface. The error in the velocity measurements, estimated

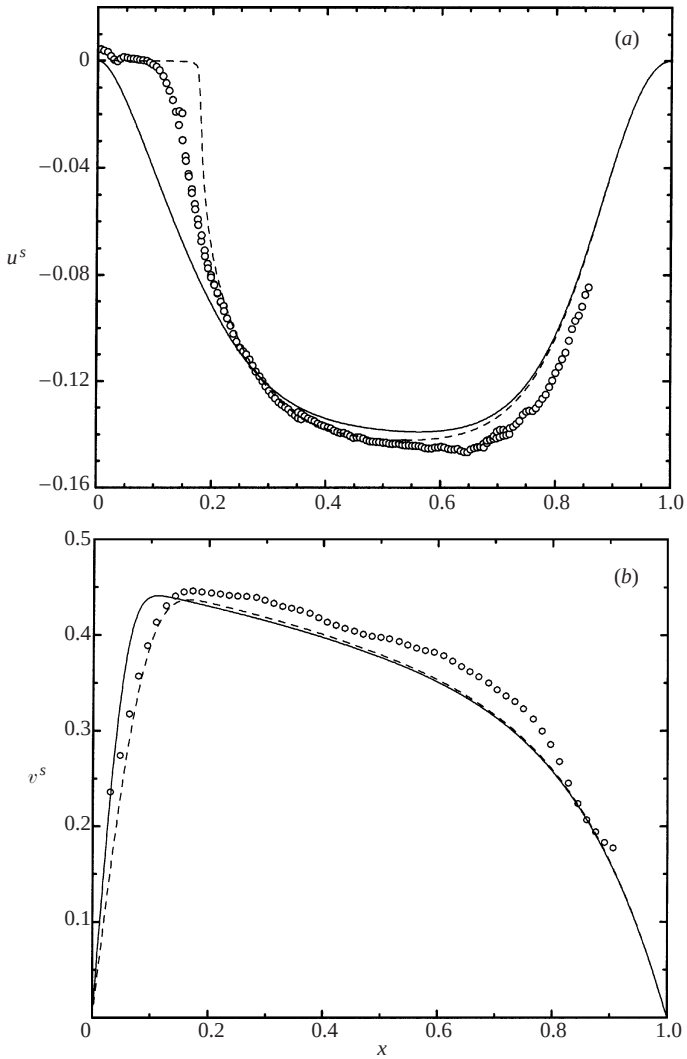

FIGURE 8. Profile of (*a*) radial velocity at the interface, $u^s(x)$, and (*b*) azimuthal velocity at the interface, $v^s(x)$, at steady state for $Re = 8500$: measurements of the clean interface (symbols), computed profiles for $c_0 = 0.0$ (solid) and $c_0 = 0.05$ (dashed).

to be $\pm 2\%$ of full scale, can account for some of the observed differences between the measurements and the computed profiles, especially in the outer region ($x > 0.6$). More importantly, the resolution of the measurements is one order of magnitude less than that of the computations, and as a result the measured velocity data represent a finite degree of depth averaging (2–4% depth averaging for the measurements cf. node spacing of 0.3% of the depth in the computations). Another factor that may contribute to the discrepancies between the measurements and computations is the variation in Reynolds number due to viscosity changes caused by uncertainty in the temperature. The uncertainty in the temperature, $\pm 1^\circ$C, represents a variation of $\pm 2.2\%$ in Reynolds number. Considering these factors, the overall agreement between the measured surface velocity components and the computations is good.

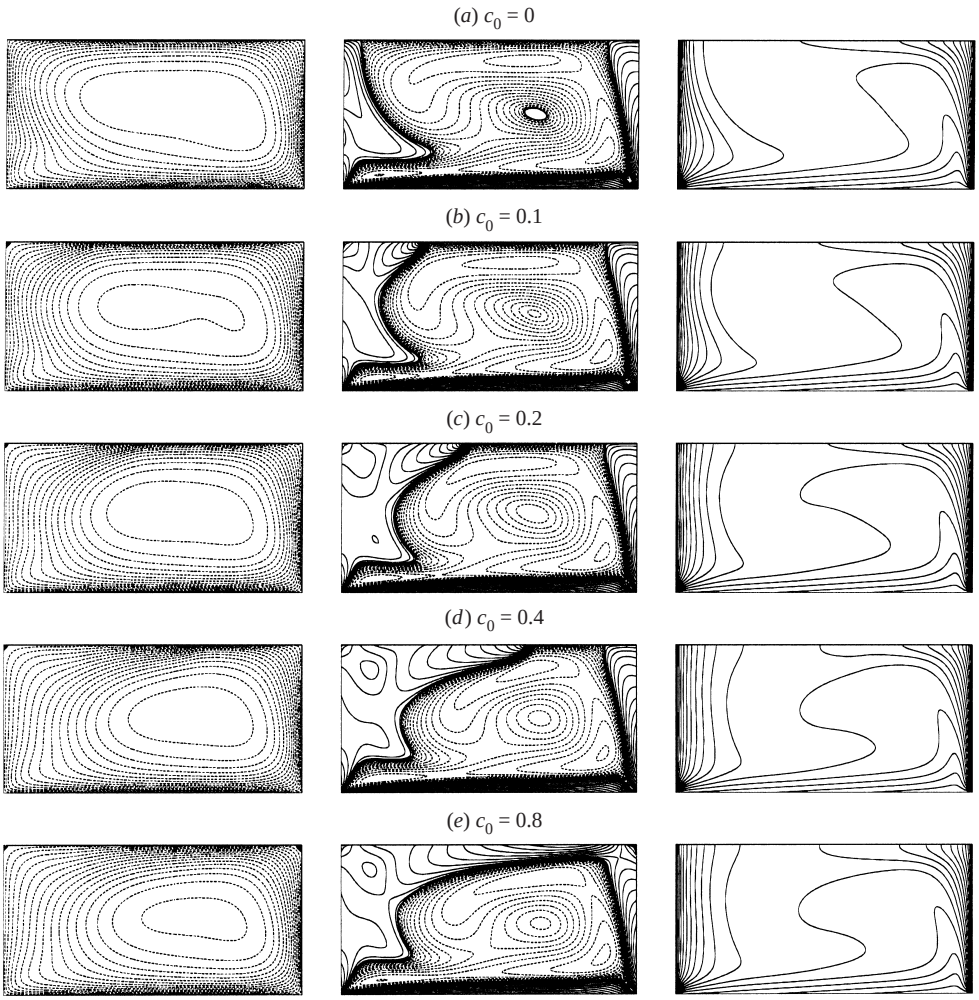

FIGURE 9. Contours of ψ (left), η (middle), and α (right), at steady state with $Re = 8500$ and initial uniform distribution of vitamin K_1 on the interface, c_0. The dashed lines are negative and solid lines are positive contours of η.

5.2. *Coupling between the interface and bulk flow*

The computed bulk flow for a range of initial surfactant concentrations, starting from a clean surface ($c_0 = 0$) is shown in figure 9. Contours of the streamfunction, ψ, azimuthal vorticity, η, and angular momentum, α, are presented. The bulk secondary flow which drives the interfacial flow is apparent in the contours of ψ. This bulk flow overturns in the counter-clockwise direction. The boundary layers on the (stationary) inner and outer cylinders, as well as the relatively strong boundary layer on the rotating bottom, are evident from the η contours. As expected for the clean case, the azimuthal vorticity decreases to zero at the surface ($z = d$) in a thin region. Note that at the surface, this component of vorticity is the radial shear stress $\partial u/\partial z$. The η contours near the interface indicate that the presence of the boundary layer on the inner cylinder is evident on the surface for x up to approximately 0.06. Further evidence of the deceleration of the radial inflow is the small recirculation zone at the corner where the surface meets the inner cylinder. This is consistent with the

measurements of u at the interface, which diminished rapidly at $x = 0.06$, indicating that residual surfactants covered the surface up to approximately $x = 0.1$ for the case with no added surfactants ($c_0 = 0$). This suggests that even a minute amount of residual surfactant can remain spread in that region.

For finite c_0, figure 9 shows that a boundary layer forms at the air/water interface. For $c_0 < 0.8\,\mathrm{mg\,m^{-2}}$ the secondary flow near the surface is strong enough to compress the monolayer towards the inner cylinder and clean a portion of the surface, forcing the leading edge of the free-surface boundary layer to the left. The meridional bulk flow, as depicted by the streamlines, slows down considerably beneath the surface boundary layer (in fact $u \to 0$ as $z \to d$), but is accelerated compared to the clean case beneath the portion of the surface that has been swept clean of the surfactant. This is in agreement with the measurements (see figure 5). The state of the interface changes the entire bulk flow structure, not just in the neighbourhood of the interface. This is most notable in the boundary layer structure on the inner cylinder all the way down to the rotating bottom. Also, the change imparted to the bulk meridional circulation by the presence of surfactants has a pronounced influence on the way the vortex lines (contours of α) are advected into the interior; their axial gradients directly affect η in the interior (through the $(-1/r^3)\partial\alpha^2/\partial z$ term in (4.4)). This then directly feeds back into the meridional flow (ψ) through (4.5). So the nonlinear coupling between the interface and the bulk flow is manifest throughout the entire flow field.

The initial condition at the interface is of a uniform monolayer of concentration c_0. So, initially, $\partial\sigma/\partial r = 0$ and surfactants are swept radially inwards by the bulk radial flow at the interface. Two things happen as the monolayer is swept inwards: (i) a concentration gradient develops, $\partial c/\partial r < 0$, and (ii) the concentration builds up at smaller r so that the part of the equation of state that is in play has larger gradients, $\partial\sigma/\partial c < 0$. For small c_0, the surfactants can be swept until the combination $(\partial\sigma/\partial c)\partial c/\partial r$, i.e. the Marangoni stress, is large enough to resist any further build-up of surfactants. At this point, a contamination front is established. In figure 10 are plotted at steady state the concentration profiles for $Re = 8500$ over a range of c_0. For very small c_0 ($\sim 0.05\,\mathrm{mg\,m^{-2}}$), almost the entire surface is swept clean of surfactants; for larger c_0 the extent of the cleansing is diminished, and for $c_0 \geqslant 0.8\,\mathrm{mg\,m^{-2}}$ there is no cleaning, although the bulk radial flow is still able to compress the monolayer to some degree. The location of the contamination front depends critically on the nonlinear form of the equation of state and the strength of the bulk radial flow at the interface (essentially measured by Re and $\Lambda = d/(r_o - r_i)$). Near the interface, u^s generally increases with increasing Re and decreasing Λ. The uncertainty in the experimental determination of $\sigma(c)$, particularly in the measurement of c ($\pm 5\%$ error), is enough to account for the differences between the measured and computed flows. Another factor to consider when comparing the experiments with a deposited monolayer and the calculations is the small, but finite, amount of residual surfactant in the bulk in the experiment that may interact with the vitamin K_1 monolayer. The effect of a soluble surfactant on the equilibrium surface tension of an insoluble monolayer has been studied in the past (e.g. see Sundaram & Stebe 1996). However, much less is known about the soluble/insoluble interaction in flowing systems.

At the contamination front, there is essentially a shock in c (it is not a discontinuity due to the finite surface diffusivity, Pe^s), and this leads to a large spike in the surface shear stress, as seen in the profiles of η^s (figure 11). The width of this spike scales with $1/\sqrt{Pe^s}$. From the figure, it can be seen that behind the spike where the monolayer resides, η^s relaxes to a distribution corresponding to η^s for $c_0 \geqslant 0.8$, i.e. the η^s of any case with no surface cleaning. Also, behind the front, $u^s \to 0$ (see figure 12*a*). However,

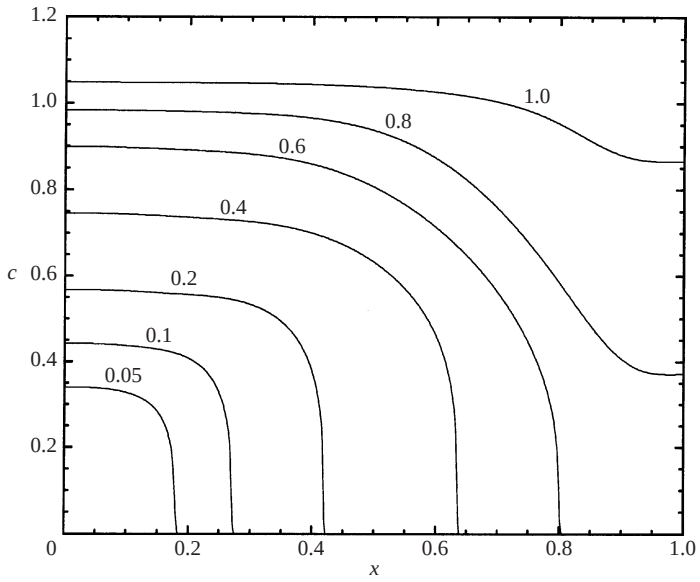

FIGURE 10. Computed profiles of surfactant concentration, $c(x)$, for c_0 as indicated, at steady state for $Re = 8500$.

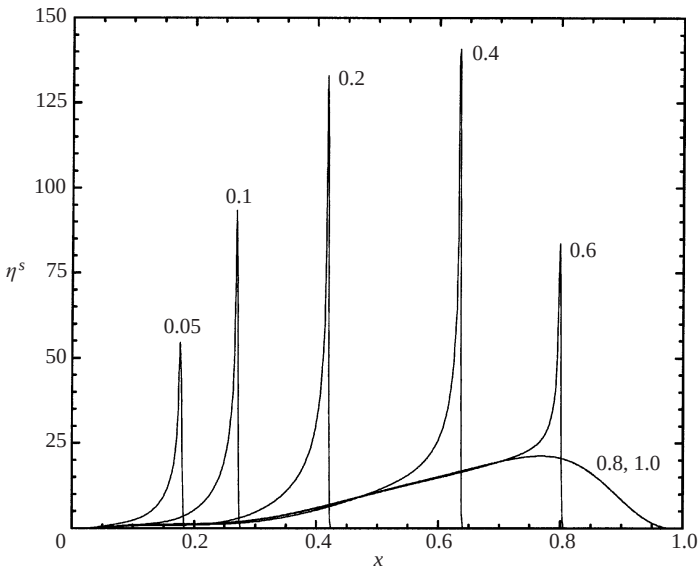

FIGURE 11. Computed profiles of azimuthal vorticity at the interface, $\eta^s(x)$, for c_0 as indicated, at steady state for $Re = 8500$.

in the azimuthal direction, since the flow is axisymmetric, there are no concentration gradients for any c_0, and the surface azimuthal velocity, v^s, for inviscid surfactant systems is not directly aware of the presence of surfactants. This is illustrated in figure 12(*b*), where v^s profiles for a range of $c_0 \in [0.0, 1.0]$ are plotted; these profiles are little affected by c_0, consistent with the measurements.

Typically when the Marangoni stress is dominating, the interface is thought of as immobile, acting as a no-slip surface. But this is only true for the velocity components

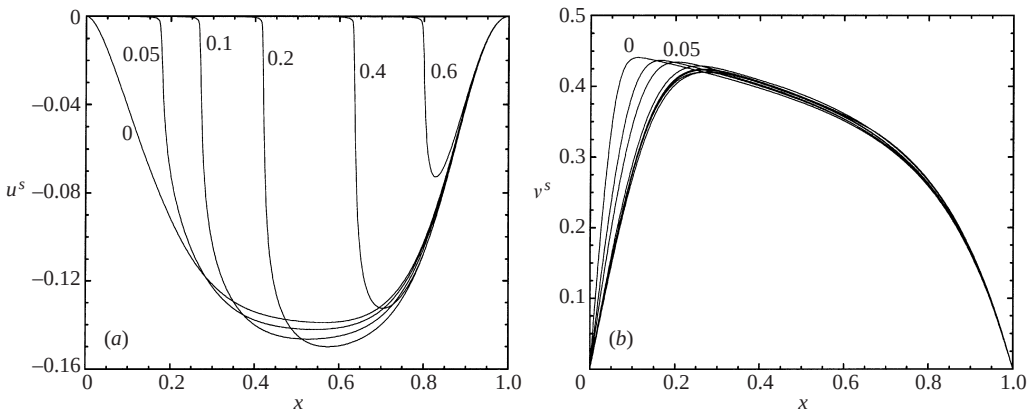

FIGURE 12. Computed profiles of (*a*) radial velocity at the interface, $u^s(x)$, and (*b*) azimuthal velocity at the interface, $v^s(x)$, for c_0 as indicated, at steady state for $Re = 8500$. In (*b*) for $c_0 > 0.2$ all profiles essentially collapse.

in the direction of the Marangoni stress. In this axisymmetric swirling flow, this direction is radial. In the azimuthal direction, since the flow is axisymmetric, there are no azimuthal gradients of surfactant, and so there are no Marangoni stresses acting in that direction. The result is that in the radial direction, the Marangoni stress makes the interface act like a no-slip surface, but in the azimuthal direction it is not immobilized. This has fundamental consequences for models of contaminated interfaces; surfactant coverage does not simply mean that the interface is no-slip.

The above considerations motivate us to consider an idealization of the interfacial stress balance to explore what role the nonlinear equation of state plays in determining the coupled interfacial/bulk flow when there is complete surfactant coverage. The idealization is that the interface condition $\eta = (1/Ca)\partial\bar{\sigma}/\partial r$ is replaced by the condition for a rigid, no-slip surface, $\eta = (-1/r)\partial^2\psi/\partial z^2$, but α continues to satisfy $\partial\alpha/\partial z = 0$; this is in contrast to the true no-slip condition which would have $\alpha = 0$ at the top. Figure 13 shows the flows at steady state for (*a*) a monolayer-covered interface with $c_0 = 1.0\,\mathrm{mg\,m^{-2}}$ (this should be compared with the $c_0 = 0.8$ case in figure 9*e*; in both cases the interface remains completely covered, but each has a very different concentration gradient distribution, as shown in figure 10, and yet the resultant flows are virtually identical), (*b*) the flow when the idealized (radially stagnant) condition was employed, and (*c*) the flow for a no-slip top. The free-surface boundary layer is qualitatively similar to the radially stagnant and no-slip top cases. Note that the contours and radial profiles at the interface of η when the surface is completely covered are virtually indistinguishable. We (Lopez & Hirsa 2000) also found this to be the case in a hemicyanine/water system; it would seem that once the interface is completely covered, the radial shear stress is independent of the details of the equation of state (the surface viscosities may still be important, but in the cases we have examined these have not been manifest for the radial stress balance). Although the vorticity contours for the $c_0 = 1.0\,\mathrm{mg\,m^{-2}}$ and the no-slip top have much in common, the vortex lines (contours of α) are very different in the two cases. In the free surface cases the vortex lines always terminate normal to the surface, since the surface shear viscosity is zero everywhere, with or without a monolayer, whereas in the solid wall case the vortex lines cannot end at the surface and are tangential to it. In the radially stagnant case however, the vortex lines behave just as

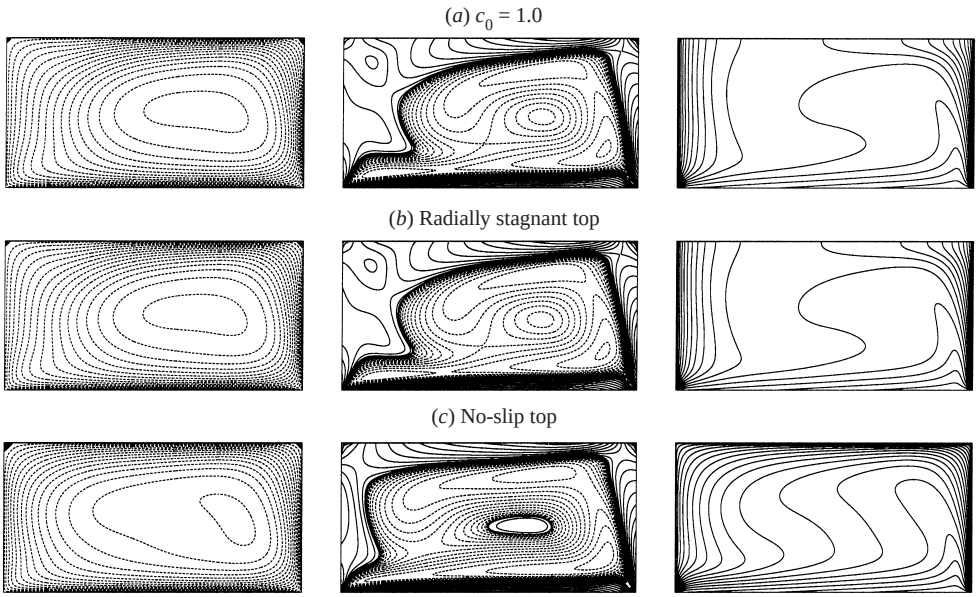

FIGURE 13. Contours of ψ (left), η (middle), and α (right), at steady state with $Re = 8500$ and (*a*) initial uniform distribution of vitamin K_1 on the interface $c_0 = 1.0\,\mathrm{mg\,m^{-2}}$, (*b*) using the radially-stagnant boundary condition on the top, and (*c*) a rigid, no-slip top. The dashed lines are negative and solid lines are positive contours of η.

in the surfactant cases with complete coverage. Once the interface is immobile in the direction of the Marangoni stress it is essentially unaware of the particulars of the surfactant that caused it to be immobile.

One of the earliest models of hydrodynamic coupling is the use of the stagnant-cap approximation (Davis & Acrivos 1966; Harper 1973; Acrivos 1983; Sadhal & Johnson 1983) in the context of a gas bubble rising in a quiescent fluid. If the bulk flow were planar two-dimensional or axisymmetric with no swirl, as is the case in almost all previous theoretical/computational studies that have implemented the stagnant-cap approximation (e.g. see He, Maldarelli & Dagan 1991; Bel Fdhila & Duineveld 1996; Takemura & Yabe 1999; Siegel 1999; Magnaudet & Eames 2000), then replacing the interfacial stress balance condition with the shear stress condition of a no-slip boundary over the part of the interface that is covered by surfactants at steady state is the appropriate thing to do. However, there are caveats to the implementation of this simplification of the interfacial coupling (e.g. also see discussion in Cuenot, Magnaudet & Spennato 1997). To begin with, the stagnant-cap approximation can only be implemented at steady state, unless certain assumptions are made about how the surfactant is dynamically distributed during temporal evolution, otherwise the location of the contamination front has to be determined dynamically. During temporal evolution, the surfactant covered portion of the interface need not have zero surface velocity even though at steady state the surfactant covered portion of the interface has $u^s = 0$. The location of the contamination front depends critically on the distribution of Marangoni stress on the interface which is determined by the precise nature of the equation of state, $\sigma(c)$, and the local thermodynamic state of the interface, $c(x)$, which in turn is determined by u^s. The other caveat on the usual implementation of the stagnant cap approximation is when the interfacial flow has a

direction along which there is no Marangoni stress but has shear (e.g. the azimuthal direction in an axisymmetric swirling flow, such as that studied here, but could also apply to axisymmetric bubbles or drops that are rotating about a symmetry axis). In these cases only the Marangoni stress should be replaced by the no-slip stress and one still needs to use the appropriate stress balance in the other direction. For vitamin K_1, the surface shear viscosity at the concentrations considered is negligible, so in the azimuthal direction the interface is stress-free. However, for surfactants with non-zero surface shear viscosity (e.g. hemicyanine and steric acid), it has been observed both experimentally (Hirsa, Harper & Kim 1995) and computationally (Lopez & Hirsa 2000) that even though there is no concentration gradient, and hence no Marangoni stress, in the azimuthal direction in axisymmetric swirling flows, the presence of a viscous monolayer imparts a shear stress to the interface resulting in significant vortex line bending at the interface. Further, even in the direction of the Marangoni stress (e.g. radial in our flow), it is still not clear what role surface viscosities (both shear and dilatational) play in determining the appropriateness of the stagnant cap approximation (i.e. the hydrodynamic coupling). In all the above considerations, we have in mind flows where the capillary number is very small so that the Marangoni contribution to the stress balance far outweighs that due to the surface viscosities. The competition between Marangoni stress and the stress due to surface viscosities remains an open question which we shall address in the near future.

6. Concluding remarks

The general agreement found between the experimental results and the computations confirms the appropriateness of the elastic and inviscid interface model for the vitamin K_1 monolayer on water in the range of c reported here. Thus, the interpretation of the equilibrium surface tension utilized in the constitutive relation (Scriven 1960) has been demonstrated in a flowing system at finite Re.

The experiments showed that even minute amounts of residual surfactants, not necessarily detectable through surface tension measurements, can exhibit surface elasticity if the interfacial velocity field is not solenoidal and the surfactants are compressed. The results also show that the details of the equation of state must be carefully considered in any theoretical study if experimentally verifiable results are to be obtained.

Several lines of research now appear attractive following this work. One interesting flow regime for the present apparatus is the high surfactant concentration regime where the surface remains completely covered (e.g. for the vitamin K_1 monolayer this would correspond to $c_0 > 0.8\,\mathrm{mg\,m^{-2}}$ when $Re \sim 8500$). In this flow regime, the tangential stress balance can be replaced by the radially stagnant condition, unless $\mu^s(c)$ is non-negligible when the surface coverage is at large concentration levels. This then offers the possibility of significantly increasing the upper bound for the range of μ^s measurable with the 'deep-channel surface viscometer', by operating it at large Re; the deep-channel surface viscometer operated at low Re is already considered the most sensitive device for the measurement of small values of μ^s (see Edwards *et al.* 1991). The cost of this added capability is that an analytical solution for the flow, obtainable in the Stokes flow limit where the viscometer is usually used, is no longer possible at finite Re and the determination of μ^s would require not only measurements of the azimuthal velocity at the surface but also numerical computations of the Navier–Stokes equations.

We would like to thank Michael J. Vogel for his assistance with many of the experiments and his insightful suggestions. Also, we would like to thank Christopher M. Tomaso for making the surface shear viscosity measurements. We also like to thank Dr Steven A. Snow of Dow-Corning for his assistance in identifying suitable seeding particles and his suggestions for particle cleaning. This work was supported by NSF Grants CTS-9803478 and CTS-9896259.

REFERENCES

Acrivos, A. 1983 The breakup of small drops and bubbles in shear flows. *Ann. N.Y. Acad. Sci.* **404**, 1–11.

Agrawal, M. L. & Neuman, R. D. 1988 Surface diffusion in monomolecular films. *J. Colloid Interface Sci.* **121**, 366–380.

Aris, R. 1962 *Vectors, Tensors, and the Basic Equations of Fluid Mechanics*. Prentice–Hall.

Bel Fdhila, R. & Duineveld, P. C. 1996 The effect of surfactant on the rise of a spherical bubble at high Reynolds and Peclet numbers. *Phys. Fluids* **8**, 310–321.

Boussinesq, J. 1913 Existence of a superficial viscosity in the thin transition layer separating one liquid from another contiguous fluid. *C. R. Hehd. Seances Acad. Sci.* **156**, 983–989.

Chen, J. & Stebe, K. J. 1996 Marangoni retardation of the terminal velocity of a settling droplet: The role of surfactant physico-chemistry. *J. Colloid Interface Sci.* **178**, 144–155.

Cuenot, B., Magnaudet, J. & Spennato, B. 1997 The effects of slightly soluble surfactants on the flow around a spherical bubble. *J. Fluid Mech.* **339**, 25–53.

Davis, R. E. & Acrivos, A. 1966 The influence of surfactants on the creeping flow of bubbles. *Chem. Engng Sci.* **21**, 681–687.

Edwards, D. A., Brenner, H. & Wasan, D. T. 1991 *Interfacial Transport Processes and Rheology*. Butterworth-Heinemann.

Eggleton, C. E., Pawar, Y. P. & Stebe, K. J. 1999 Insoluble surfactants on a drop in an extensional flow: a generalization of the stagnated surface limit to deforming interfaces. *J. Fluid Mech.* **385**, 79–99.

Gaines, G. L. 1966 *Insoluble Monolayers at Liquid-Gas Interfaces*. Interscience.

Grotberg, J. B. 1994 Pulmonary flow and transport phenomena. *Ann. Rev. Fluid Mech.* **26**, 529–571.

Harper, J. F. 1973 Bubbles with small immobile adsorbed films rising in liquids at low Reynolds-numbers. *J. Fluid Mech.* **58**, 539–545.

He, Z., Maldarelli, C. & Dagan, Z. 1991 The size of stagnant caps of bulk soluble surfactants on the interfaces of translating fluid droplets. *J. Colloid Interface Sci.* **146**, 442–451.

Hirsa, A., Harper, J. E. & Kim, S. 1995 Columnar vortex generation and interaction with a clean or contaminated free surface. *Phys. Fluids* **7**, 2532–2534.

Hirsa, A., Korenowski, G. M., Logory, L. M. & Judd, C. D. 1997*a* Determination of surface viscosities by surfactant concentration and velocity measurements for an insoluble monolayer. *Langmuir* **13**, 3813–3822.

Hirsa, A., Korenowski, G. M., Logory, L. M. & Judd, C. D. 1997*b* Velocity field and surfactant concentration measurement techniques for free-surface flows. *Exps. Fluids* **22**, 239–248.

Hirsa, A., Vogel, M. J. & Gayton, J. D. 2001 Digital particle velocimetry technique for free-surface boundary layer measurements: Application to vortex pair interactions. *Exps. Fluids* **31** (in press).

Johnson, R. A. & Borhan, A. 1999 Effect of insoluble surfactants on the pressure-driven motion of a drop in a tube in the limit of high surface coverage. *J. Colloid Interface Sci.* **218**, 184–200.

Logory, L. M., Hirsa, A. & Anthony, D. G. 1996 Interaction of wake turbulence with a free surface. *Phys. Fluids* **8**, 805–815.

Lopez, J. M. & Chen, J. 1998 Coupling between a viscoelastic gas/liquid interface and a swirling vortex flow. *J. Fluids Engng* **120**, 655–661.

Lopez, J. M. & Hirsa, A. 1998 Direct determination of the dependence of the surface shear and dilatational viscosities on the thermodynamic state of the interface: Theoretical foundations. *J. Colloid Interface Sci.* **206**, 231–239.

Lopez, J. M. & Hirsa, A. 2000 Surfactant influenced gas/liquid interfaces: Nonlinear equation of state and finite surface viscosities. *J. Colloid Interface Sci.* **229**, 575–583.

Magnaudet, J. & Eames, I. 2000 The motion of high-Reynolds-number bubbles in inhomogeneous flows. *Ann. Rev. Fluid Mech.* **32**, 659–708.

Mannheimer, R. J. & Schechter, R. S. 1970 An improved apparatus and analysis for surface rheological measurements. *J. Colloid Interface Sci.* **32**, 195–211.

Sacchetti, M., Yu, H. & Zografi, G. 1993 Hydrodynamics coupling of monolayers with subphase. *J. Chem. Phys.* **99**, 563–566.

Sadhal, S. S. & Johnson, R. E. 1983 Stokes flow past bubbles and drops partially coated with thin films. Part 1. Stagnant cap of surfactant films: exact solution. *J. Fluid Mech.* **126**, 237–250.

Schwartz, D. K., Knobler, C. M. & Bruinsma, R. 1994 Direct observation of Langmuir monolayer flow through a channel. *Phys. Rev. Lett.* **73**, 2841–2844.

Scott, J. C. 1975 The preparation of water for surface-clean fluid mechanics. *J. Fluid Mech.* **69**, 339–351.

Scriven, L. E. 1960 Dynamics of a fluid interface. *Chem. Engng. Sci.* **12**, 98–108.

Siegel, M. 1999 Influence of surfactant on rounded and pointed bubbles in two-dimensional Stokes flow. *SIAM J. Appl. Math.* **59**, 1998–2027.

Slattery, J. C. 1990 *Interfacial Transport Phenomena*. Springer-Verlag.

Snow, S. A., Pernisz, U. C. & Stevens, R. E. 1998 Thin liquid model polyurethane films. In *Proceedings of the 1998 Polyurethane World Congress*, p. C4.

Stone, H. A. & Ajdari, A. 1998 Hydrodynamics of particles embedded in a flat surfactant layer overlying a subphase of finite depth. *J. Fluid Mech.* **369**, 151–173.

Stone, H. A. & Leal, L. G. 1990 The effects of surfactants on drop deformation and breakup. *J. Fluid Mech.* **220**, 161–186.

Sundaram, S. & Stebe, K. J. 1996 Equations for the equilibrium surface pressure increase on the penetration of an insoluble monolayer by a soluble surfactant. *Langmuir* **12**, 2028–2034.

Takemura, F. & Yabe, A. 1999 Rising speed and dissolution rate of a carbon dioxide bubble in slightly contaminated water. *J. Fluid Mech.* **378**, 319–334.

Trygvasson, G., Abdollahi-Alibeik, J., Willmarth, W. W. & Hirsa, A. 1992 Collision of a vortex pair with a contaminated free surface. *Phys. Fluids* **4**, 1215–1229.

Tsai, W.-T. & Yue, D. K. P. 1995 Effects of soluble and insoluble surfactant on laminar interactions of vortical flows with a free-surface. *J. Fluid Mech.* **289**, 315–349.

Vogel, M. J., Hirsa, A. H., Kelley, J. S. & Korenowski, G. M. 2001 Simultaneous measurement of free-surface velocity and surfactant concentration via a common laser probe. *Rev. Sci. Inst.* **72**, 1502–1509.

Warncke, A., Gharib, M. & Roesgen, T. 1996 Flow measurements near a Reynolds ridge. *J. Fluids Engng* **118**, 621–624.

Weast, B. (Ed.) 1980 *Handbook of Chemistry and Physics*, 60th Edn. CRC.

Weitzel, G., Fretzdorff, A.-M. & Heller, S. 1956 Grenzflächenuntersuchungen an Tokopherol-Verbindungen und am Vitamin K_1. *Hoppe-Seylers Z. Physiol. Chem.* **303**, 14–26.